

Modulating the electronic properties of perovskite via σ - π interfacial interactions: A computational study

Cite as: APL Mater. 6, 114203 (2018); <https://doi.org/10.1063/1.5044453>

Submitted: 13 June 2018 . Accepted: 02 August 2018 . Published Online: 12 September 2018

Fengyu Li, Fuzhao Yi, Junfeng Gao, Haijun Zhang, and Zhongfang Chen



View Online



Export Citation



CrossMark

ARTICLES YOU MAY BE INTERESTED IN

Octahedral connectivity and its role in determining the phase stabilities and electronic structures of low-dimensional, perovskite-related iodoplumbates

APL Materials 6, 114202 (2018); <https://doi.org/10.1063/1.5046404>

Structural evolution and photoluminescence properties of a 2D hybrid perovskite under pressure

APL Materials 6, 114201 (2018); <https://doi.org/10.1063/1.5012645>

Magnetic functionality of thin film perovskite hybrid

APL Materials 6, 114203 (2018); <https://doi.org/10.1063/1.5042323>

additive manufacturing crystal growth cerium oxide polishing powder silver nanoparticles sputtering targets III-IV semiconductors CVD precursors europium phosphors

AMERICAN ELEMENTS

THE ADVANCED MATERIALS MANUFACTURER®

deposition LEDs Lighting spintronics solar energy osmium carbons thin films chalcogenides AuNPs

Gd lithium battery electrolytes 99.999% ruthenium spheres

graphical fullerenes copper nanoparticles diamond micropowder

MBE grade materials palladium catalysts flexible electronics

barium borate borosilicate glass dysprosium pellets YBCO

pyrolytic graphite 3d graphene foam indium tin oxide mesoporous silica

raman substrates sapphire windows tungsten carbide InGaAs

barium fluoride carbon nanotubes lithium niobate scandium powder

gallium lump glassy carbon nanodispersions

surface functionalized nanoparticles organometallics quantum dot

III-V wafers laser crystals ultra high purity materials MOFs

rare earth metals photovoltaics refractory metals MOCVD

superconductors transparent ceramics ultra high purity silicon

American Elements opens up a world of possibilities so you can **Now Invent!**

Over 15,000 certified high purity laboratory chemicals, metals, & advanced materials and a state-of-the-art Research Center. Printable GHS-compliant Safety Data Sheets. Thousands of new products. And much more. All on a secure multi-language "Mobile Responsive" platform.

perovskite crystals yttrium iron garnet alternative energy h-BN

gold nanocubes graphene oxide macromolecules photonics

rhodium sponge fiber optics beamsplitters infrared dyes zeolites

fused quartz metallocenes platinum ink buckyballs Ti-6Al-4V

Now Invent.™
The Next Generation of Material Science Catalogs

www.americanelements.com

Modulating the electronic properties of perovskite via σ - π interfacial interactions: A computational study

Fengyu Li,^{1,2,a} Fuzhao Yi,² Junfeng Gao,³ Haijun Zhang,⁴
and Zhongfang Chen^{2,a}

¹Physical School of Science and Technology, Inner Mongolia University,
Hohhot 010021, China

²Department of Chemistry, University of Puerto Rico, Rio Piedras Campus, San Juan,
Puerto Rico 00931, USA

³Key Laboratory of Materials Modification by Laser, Ion and Electron Beams,
Dalian University of Technology, Ministry of Education, Dalian 116024, China

⁴Center for Aircraft Fire and Emergency, Civil Aviation University of China,
Tianjin 300300, China

(Received 13 June 2018; accepted 2 August 2018; published online 12 September 2018)

By means of density functional theory computations, we comprehensively investigated the stability and electronic properties of the hybrid $\text{CH}_3\text{NH}_3\text{PbI}_3$ (methylammonium lead iodide, MAPI)/graphene heterojunctions, where the MAPI layer was adopted with MAI (methylammonium iodide)-terminations. Our computations demonstrated that the σ - π interfacial interactions make the contact very stable, and such interactions lead to charge redistribution and concomitant internal electric field in the interface, which is beneficial for the electron-hole separation. © 2018 Author(s). All article content, except where otherwise noted, is licensed under a Creative Commons Attribution (CC BY) license (<http://creativecommons.org/licenses/by/4.0/>). <https://doi.org/10.1063/1.5044453>

The methyl ammonium lead iodide ($\text{CH}_3\text{NH}_3\text{PbI}_3$, MAPI) perovskites, as one organic metal halide perovskite, are making record-breaking advances in the power conversion efficiency (PCE) of nanostructured solar cells: the PCE value increased from 3.81% for the dye-sensitized solar cells in 2009¹ to 10.1% for the Sn doped perovskite materials in 2014² and to 19.3% for the perovskite heterojunction in 2014³ and recently exceeded 20% for hybrid perovskite solar cells.⁴⁻⁶ It has been recognized that the interface structure is playing an important role in the PCE of perovskite-based solar cells.⁷⁻¹⁷ In recent years, tremendous theoretical efforts have been devoted to understanding the underlying mechanisms of the superior and the unique electronic properties of perovskites and 2D heterojunctions.¹⁸⁻³⁰ For example, density functional theory (DFT) studies of Volonakis and Giustino verified that the interfacial ferroelectricity of graphene-MAPbI₃ interfaces originates from the interplay between the graphene plane and the MAPbI₃'s octahedral connectivity.²² Haruyama *et al.*²⁴ examined the effects of vacancy defect on the interface of anatase-TiO₂(001) and tetragonal MAPbI₃(110) and found that vacancies in the TiO₂ layer create hole trap states and recombination centers. DFT calculations of Hu *et al.* revealed that the band edge modulations in the graphene/ $\text{CH}_3\text{NH}_3\text{PbI}_3$ heterojunctions are due to the interfacial charge redistribution.³⁰ Note that the 2D lateral heterostructures also hold a wide potential for device applications.³¹

However, most theoretical investigations concentrated on the PbI₂-terminated interfaces,^{22,24,30} and the interfaces of MAI (methylammonium iodide) terminations were scarcely explored. The recent theoretical study of Wang *et al.* revealed that both the Pd atoms and the MA molecules of the MA-terminated MAPbI₃ surface play essential roles in the photocatalytic hydrogen evolution reaction.³² Considering the availability of vast σ bonds in the MAI-terminated MAPI surfaces and the strong effect of σ - π interfacial interactions (Fig. 1) on the electronic structures of graphene,³³ here by

^aAuthors to whom correspondence should be addressed: fengyuli@imu.edu.cn and zhongfangchen@gmail.com

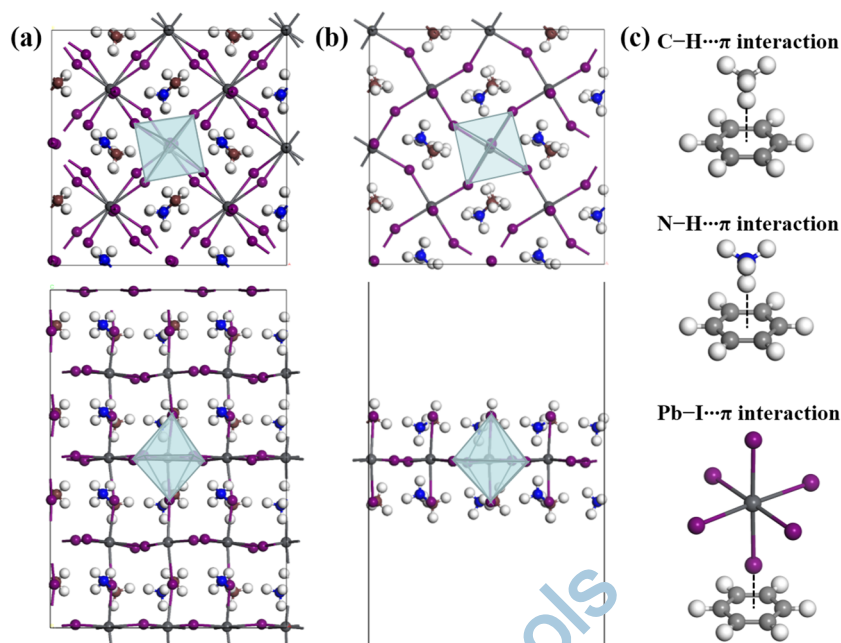


FIG. 1. Top (up) and side (bottom) views of the MAPI bulk (a) and a 2D single layer (b) models used in this work. Color scheme: H, white; C, brown; N, blue; I, purple; Pb, dark gray. The PbI₃ octahedron was highlighted in light blue. (c) Illustration of the three types of σ - π interfacial interactions in the heterostructure of the MAI-terminated MAPI slab and graphene.

means of DFT computations, we studied the stability and electronic properties of the heterojunctions of the MAPI with MAI terminations and graphene (MAPI/G).

Our DFT calculations were carried out using the Vienna *ab initio* simulation package (VASP) code.³⁴ Considering the weak interactions between MAPI and graphene monolayers, optPBE-vdW functional³⁵ was used for geometry optimizations. For the band structure computations, we employed the PBE (Perdew-Burke-Ernzerhof) functional since it yields a 1.73 eV bandgap for MAPI bulk, in good agreement with the experimental values of 1.5–1.7 eV.^{36,37} Based on recent studies using the quasi-particle GW method,^{38,39} the good agreement between the computed PBE and the measured bandgap is a result of error cancellation, i.e., an underestimation due to the standard DFT bandgap error and an overestimation due to the exclusion of spin-orbit coupling (SOC). Recently, Agiorgousis *et al.* found that the change in the calculated atomic forces is negligibly small when including the SOC.⁴⁰ From our test calculations on a MAPI slab, we found that including the SOC has non-ignorable influence on the band structure of the MAPI slab (Fig. 2). Thus, SOC was considered in our band structure calculations for comparison.

The Monkhorst-Pack scheme⁴¹ of $8 \times 8 \times 1$ ($4 \times 4 \times 1$) k-point mesh was applied for unit cell ($2 \times 2 \times 1$ supercell) geometry optimizations, while a larger grid ($25 \times 25 \times 1$) was used for electronic

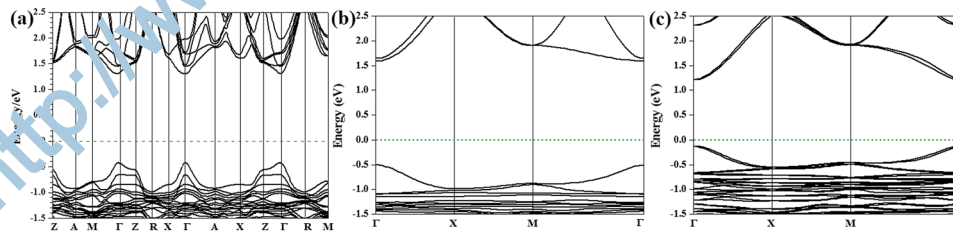


FIG. 2. Calculated band structures of (a) the MAPI bulk (unit cell), (b) the MAPI monolayer without SOC, and (c) the MAPI monolayer with SOC along the high-symmetry lines in the first Brillouin zone using PBE. The Fermi level was set to be zero as denoted by the green dashed line.

structure computations. The kinetic energy cutoff for the plane-wave basis set was chosen to be 500 eV. The MAPI monolayer model was built based on the experimentally measured lattice constants of the tetragonal bulk MAPI ($I4/mcm$) [$a = b = 8.86 \text{ \AA}$, $c = 12.66 \text{ \AA}$; Fig. 1(a)].⁴² The vacuum along the c -axis was set larger than 20 \AA , which is sufficient to avoid the interaction between neighboring slabs.

In our study, the binding energy between MAPI and graphene monolayers, E_b , is defined as $E_b = E(\text{MAPI/G}) - E(\text{MAPI}) - E(\text{G})$, where $E(\text{MAPI/G})$, $E(\text{MAPI})$, and $E(\text{G})$ are the total energies of MAPI/G and the energies of MAPI and graphene single layers, respectively. According to this definition, a more negative binding energy indicates a more energetically favorable interaction between MAPI and graphene.

We first studied the free-standing MAPI slab. For the MAI-terminated slab, each $[\text{PbI}_6]^{4-}$ octahedron is connected with four neighbors at the halide in the periodic plane, and the PbI_2 -plane is sandwiched between two MAI layers (Fig. 1). The lengths of two Pb—I dangling bonds ($3.26, 3.27 \text{ \AA}$) are slightly longer than those four in the plane ($3.18, 3.20, 3.21, 3.22 \text{ \AA}$) due to the Jahn-Teller effect.⁴³ Both surfaces are terminated with CH_3NH_3^+ and I atoms.

The energy difference between spin-polarized and spin-nonpolarized calculations is less than 0.5 meV per unit cell ($\text{C}_4\text{N}_4\text{H}_{24}\text{Pb}_2\text{I}_8$), and the magnetic moment is $0.00\mu_B$; thus the spin-nonpolarized computations were used for the electronic properties of the MAPI monolayer and MAPI/graphene hybrids.

To evaluate the stability of MAPI with MAI termination, we calculated the cohesive energy per atom (E_c) using the following definition: $E_c = (iE_C + jE_N + kE_H + mE_I + nE_{Pb} - E_{\text{MAPI}})/(i + j + k + m + n)$, where E_C , E_N , E_H , E_I , E_{Pb} , and E_{MAPI} represent the total energies of the isolated atoms (C, N, H, I, and Pb) and MAPI slab, respectively, and i , j , k , n , and m correspond to the number of isolated atoms in the slab. Previous theoretical studies revealed that the 2D MAPI surfaces with the stable vacant termination and the PbI_2 -rich flat termination have quite comparable stability.¹⁹ For our model with MA termination, the cohesive energy (3.32 eV/atom) is larger than that of the PbI_2 -rich flat terminations (3.02 eV/atom), indicating the higher thermodynamic stability of the MAI-terminated MAPI slab. Our results are in good agreement with the DFT finding of Quarti *et al.*²⁵

The calculated band structures of the MAPI slab and bulk along high symmetry directions in the Brillouin zone are shown in Fig. 2. Both systems are indirect-bandgap semiconductors with the minimum bandgap at the Γ symmetry point. The PBE bandgap of the 2D MAPI slab with MAI termination (2.17 eV) is wider than that of the bulk (1.73 eV) and also wider than that of the PbI_2 -terminated slabs at the same theoretical level with similar settings (1.50 eV in Ref. 26, 1.56 eV in Ref. 19, 1.64 eV in Ref. 30, and 1.79 eV in Ref. 22). In comparison, the PBE + SOC yields a narrower gap value of 1.35 eV for the 2D MAPI slab.

We further examined the partial charge densities associated with the valence band maximum (VBM) and conduction band minimum (CBM) of the MAPI monolayer. As shown in Fig. 3, both the VBM and CBM consist mostly of I-5p and Pb-6p orbitals, exhibiting very similar electronic

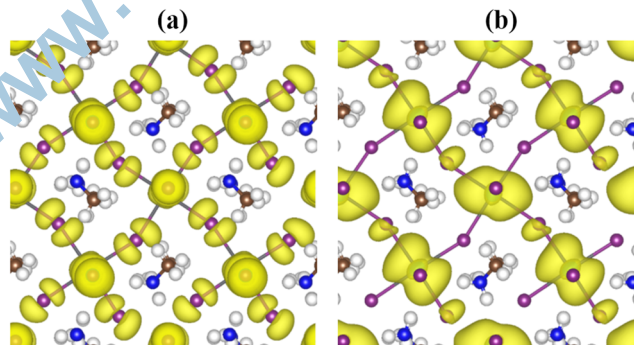


FIG. 3. Top views of VBM (a) and CBM (b) of the MAPI monolayer. Color scheme: H, white; C, light gray; N, blue; I, brown; Pb, dark gray.

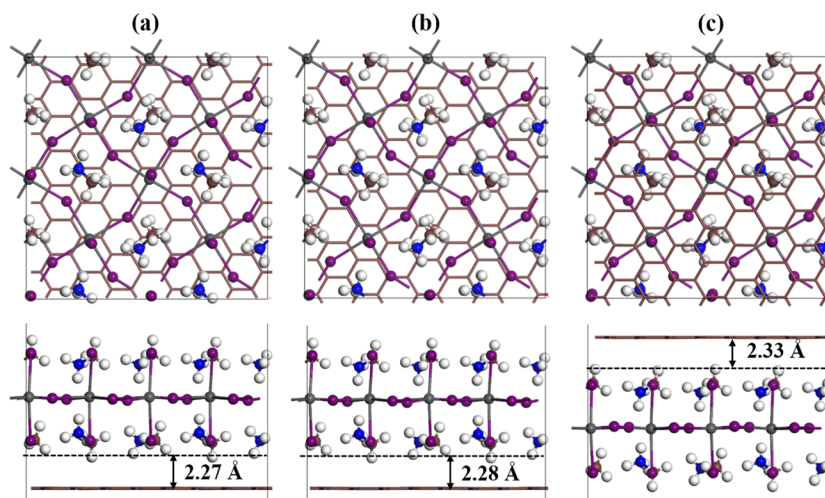


FIG. 4. Top (upper) and side (bottom) views of optimized structures of the MAPI/G bilayer in the stacking pattern of **I** (a), **II** (b), and **III** (c). Color scheme: H, white; C, light gray; N, blue; I, brown; Pb, dark gray.

characteristics as the bulk phase¹⁸ and the MAPI slabs with the stable vacant termination and the PbI_2 -rich flat termination.²⁰

For the hybrid MAPI/G bilayer, the heterojunction contains a 2×2 MAI-terminated MAPI slab ($\text{C}_{16}\text{N}_{16}\text{H}_{96}\text{Pb}_8\text{I}_{32}$) and a $4\sqrt{3} \times 7$ graphene monolayer (C_{112}). The lattice of graphene is stretched by less than 4% to match that of MAPI. Considering the asymmetry of the two MAPI surfaces, we examined three different stacking patterns (Fig. 4). To achieve a more stable interface, more σ - π interfacial interactions are desired. Thus, the MAPI slab and graphene are stacked with as much as C-H/N-H/Pb-I bonds pointing to the C_6 centers: In patterns **I** and **II**, the graphene is stacked under MAPI with as much as σ - π interfacial interactions; in pattern **III**, the MAPI is adjusted under the graphene with as much as σ - π interfacial interactions. The difference between **I** and **II** is the individual numbers of C-H and Pb-I bonds pointing to the C_6 centers, but the total number of such bonds in the two configurations are comparable.

To get the lowest-energy configuration for each stacking pattern, we plotted the binding energy (E_b) curves of the three stacking patterns (Fig. 5). The optimal distances between the outmost H layer and graphene are 2.27, 2.28, and 2.33 Å, respectively, for **I**, **II**, and **III** patterns. The lengths of two Pb-I dangling bonds (3.20–3.24 Å) are shortened up on contacting with the graphene.

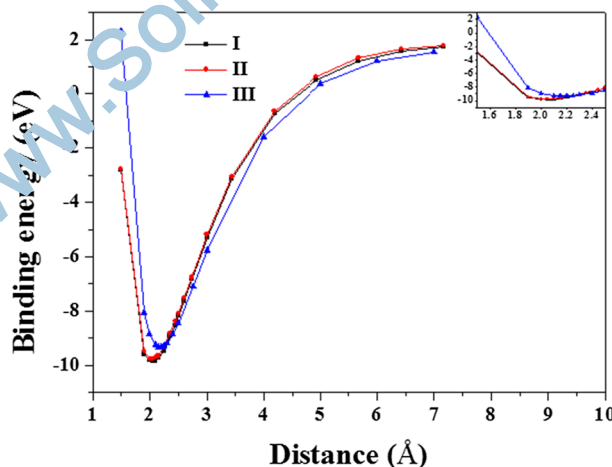


FIG. 5. Binding energy curves of the MAPI/G bilayer with three different stacking patterns.

The binding energies of these three patterns are close: **I** is energetically most favorable ($E_b = -9.90$ eV), which is closely followed by **II** ($E_b = -9.86$ eV), while **III** ($E_b = -9.44$ eV) is 0.46 eV higher in energy than **I**. The average binding strength (given by E_b/A , where A is the surface area) between the MAPI slabs with MAI termination ($3.01\text{--}3.15$ eV/nm²) is much stronger than that of PbI₂-terminated slabs ($1.38\text{--}1.47$ eV/nm²),³⁰ suggesting even stronger interfacial contact between the MAI-terminated MAPI slab and graphene. Note that both the equilibrium interlayer distances and the binding energies in MAPI/G bilayers are very close to the corresponding values in the graphene/C₄H bilayers,³³ where considerable C—H... π interactions between graphene and its partially hydrogenated counterpart (C₄H) exist.

According to the Hirshfeld charge analysis, there is a charge transfer of 0.36, 0.35, and 0.32 *l* from the graphene to the MAPI slab in systems **I**, **II**, and **III**, respectively, i.e., the graphene gains electrons and the MAPI loses electrons at the interface. This finding resembles the previous DFT findings that the π -conjugated Lewis base⁴⁴ and C₆₀²⁵ can extract electrons from the perovskite layers. We further analyzed the electron localization function (ELF).⁴⁵ Since the three MAPI/G bilayers have very similar electronic properties, here we used only bilayer **I** as the representative. As shown in Figs.6(a) and 6(b), there are more electrons distributed on the free termination of the MAPI slab than on the MAI termination of the MAPI/graphene interface, in line with the result of the Hirshfeld charge analysis.

The aforementioned charge redistribution on the MAPI-G hybrid should lead to an internal electric field along the direction pointing from the free-standing of the MAPI slab to the graphene. As expected, our computations showed that an electrostatic potential difference ($\Delta\phi$) between the free-standing MAPI surface and the graphene surface of 0.21 eV is introduced [Fig.6(c)], which is beneficial for electron-hole separation. The SOC included PBE gives very close $\Delta\phi$ value (0.22 eV).

Furthermore, we carried out the electronic band structure calculations of the MAPI/G bilayer. For comparison, we also calculated the band structure of free-standing graphene (a $4\sqrt{3} \times 7$ supercell). As shown in Fig.7, the Dirac point falls inside of the bandgap of the MAPI slab, implying that the MAPI/G bilayer is a Schottky junction. By comparing the band structures of the MAPI slab [Fig.2(b)], we found that the contact with graphene has negligible influence on the bandgap of the MAPI slab (~ 2.17 eV before and after contact). The band bending (Δ) can be estimated by the energy difference between the Fermi levels of the MAPI/G bilayer and the free-standing MAPI slab, i.e., $\Delta = \Delta E_F = W_{\text{MAPI/G}} - W_{\text{MAPI}}$, where ΔE_F is the difference of the Fermi level and $W_{\text{MAPI/G}}$ and

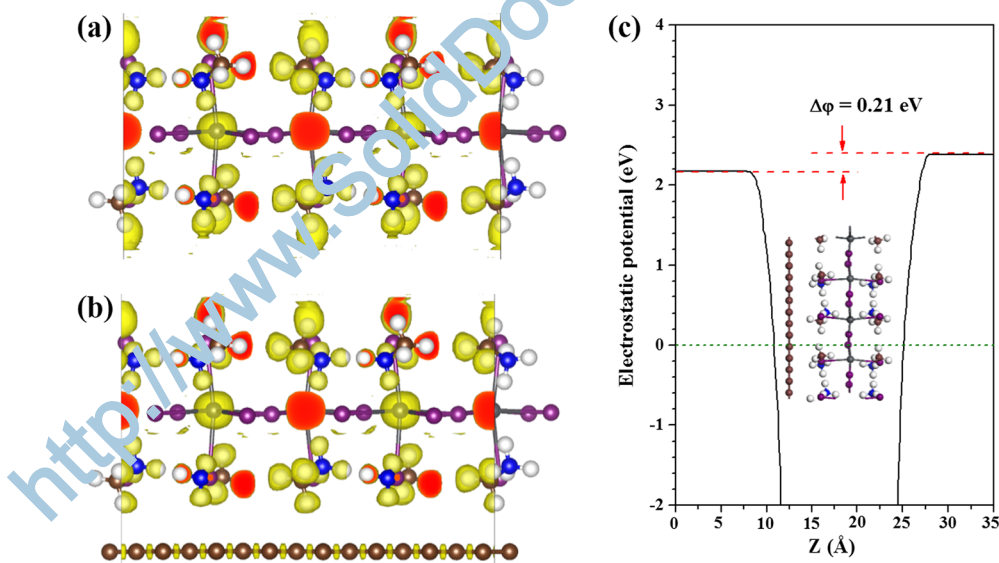


FIG. 6. The ELF (electron localization function) of the MAPI slab (a) and MAPI/G bilayer (b). (c) The surface potential difference of the MAPI/G bilayer. Color scheme: H, white; C, light gray; N, blue; I, brown; Pb, dark gray.

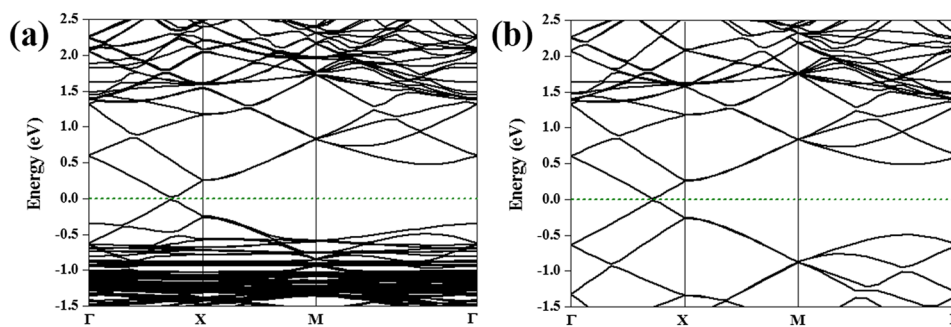


FIG. 7. PBE band structures of the (a) MAPI/G bilayer and (b) free-standing graphene. The Fermi level was assigned at 0 eV.

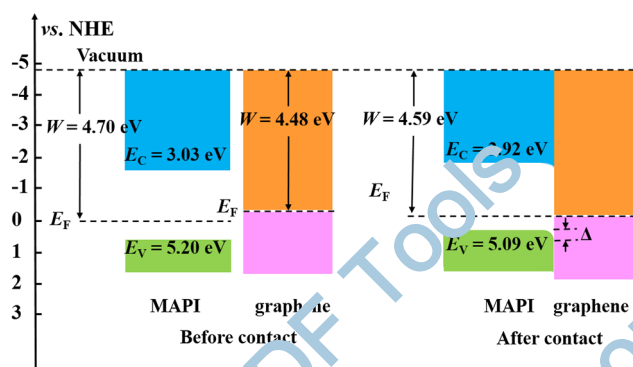


FIG. 8. PBE energy diagrams for the free-standing MAPI layer and graphene in the MAPI/G bilayer before and after contact.

W_{MAPI} are the work functions of the MAPI/G bilayer and free-standing MAPI slab, respectively. The work function of the MAPI slab and graphene is 4.70 and 4.48 eV, respectively, which indicates that the Fermi level of MAPI shifts up, while the Fermi level of graphene shifts down to reach the same value in the MAPI/G complex. Meanwhile the conduction band (CB) and valence band (VB) of the MAPI slab are both pulled downward slightly and both form a band bending of 0.21 eV at the interface. The energies of the VB maximum (E_V) and the CB minimum (E_C) of the free-standing MAPI slab are -5.20 and -3.03 eV, respectively, relative to the vacuum level. Interfacing graphene with the MAPI slab introduces the upshift of 0.11 eV for VB and CB of MAPI. Therefore, the p -type Schottky barrier height (SBH) is 0.60 eV, and the corresponding n -type SBH is 1.57 eV (Fig. 8). Since the stacking patterns only slightly affect the work function,³⁰ we did not illustrate the energy diagrams of the MAPI/G bilayer of **I** or **III** contacts here.

For the PBE + SOC calculations, the work function of the free-standing MAPI slab is 4.89 eV, and the E_V and E_C are 5.02 and 3.67 eV, respectively. In the MAPI/G complex, the work function, E_V , and E_C of MAPI turn out to be 4.68, 4.81, and 3.46 eV, respectively, and the p -type and n -type SBH will be 0.34 and 1.01 eV, respectively. The PBE method with and without SOC included gives the same trend that the p -type SBH is lower than the n -type SBH, and we only illustrate the PBE energy diagrams in Fig. 8.

In summary, by means of DFT computations, we comprehensively investigated the structural stability and electronic properties of the heterojunctions of the graphene and MAPI slab with MAI terminations. The considerable σ - π interfacial interactions endow the MAPI/G interface more stable than the contact of the PbI_2 -terminated MAPI and graphene, and the concomitant charge redistribution introduces an internal electric field in contact, which is beneficial for electron-hole separation. Though the low p -SBH obtained in the contact of the graphene and MAI-terminated MAPI slab is smaller than that of the PbI_2 -terminated interface (0.85 eV in Ref. 22), the introduction of σ - π interfacial interactions may provide some guidelines for experimentalists in fabricating more stable MAPI-graphene interfaces.

This work was supported in USA by the National Science Foundation-Centers of Research Excellence in Science and Technology (NSF-CREST Center) for Innovation, Research and Education in Environmental Nanotechnology (CIRE2N) (Grant No. HRD-1736093) and NASA (Grant No. 17-EPSCoRProp-0032), and in China by the startup project of Inner Mongolia University.

- ¹ A. Kojima, K. Teshima, Y. Shirai, and T. Miyasaka, "Organometal halide perovskites as visible-light sensitizers for photovoltaic cells," *J. Am. Chem. Soc.* **131**, 6050 (2009).
- ² F. Zuo, S. T. Williams, P. Liang, C. Chueh, C. Liao, and A. K. Jen, "Binary-metal perovskites toward high-performance planar-heterojunction hybrid solar cells," *Adv. Mater.* **26**, 6454 (2014).
- ³ H. Zhou, Q. Chen, G. Li, S. Luo, T. Song, H. S. Duan, Z. Hong, J. You, Y. Liu, and Y. Yang, "Interface engineering of highly efficient perovskite solar cells," *Science* **345**, 542 (2014).
- ⁴ N. J. Jeon, J. H. Noh, W. S. Yang, Y. C. Kim, S. Ryu, J. Seo, and S. I. Seok, "Compositional engineering of perovskite materials for high-performance solar cells," *Nature* **517**, 476 (2015).
- ⁵ W. S. Yang, J. H. Noh, N. J. Jeon, Y. C. Kim, S. Ryu, J. Seo, and S. I. Seok, "High-performance photovoltaic perovskite layers fabricated through intramolecular exchange," *Science* **348**, 1234 (2015).
- ⁶ M. Saliba, T. Matsui, J.-Y. Seo, K. Domanski, J.-P. Correa-Baena, M. K. Nazeeruddin, S. M. Zakeeruddin, W. Tress, A. Abate, A. Hagfeldt, and M. Grätzel, "Cesium-containing triple cation perovskite solar cells: Improved stability, reproducibility and high efficiency," *Energy Environ. Sci.* **9**, 1989–1997 (2016).
- ⁷ L. Etgar, P. Gao, Z. Xue, Q. Peng, A. K. Chandiran, B. Liu, M. K. Nazeeruddin, and M. Grätzel, "Mesoscopic CH₃NH₃PbI₃/TiO₂ heterojunction solar cells," *J. Am. Chem. Soc.* **134**, 17396–17399 (2012).
- ⁸ R. Lindblad *et al.*, "Electronic structure of TiO₂/CH₃NH₃PbI₃ perovskite solar cell interfaces," *J. Phys. Chem. Lett.* **5**(4), 648–653 (2014).
- ⁹ M. Batmunkh *et al.*, "Solution processed graphene structures for perovskite solar cells," *J. Mater. Chem. A* **4**(7), 2605–2616 (2016).
- ¹⁰ A. Agresti *et al.*, "Graphene-perovskite solar cells exceed 18% efficiency: A stability study," *ChemSusChem* **9**(18), 2609–2619 (2016).
- ¹¹ A. Agresti *et al.*, "Graphene interface engineering for perovskite solar modules: 12.6% power conversion efficiency over 50 cm² active area," *ACS Energy Lett.* **2**(1), 279–287 (2017).
- ¹² Y. Busby, A. Agresti *et al.*, "Aging effects in interface-engineered perovskite solar cells with 2D nanomaterials: A depth profile analysis," *Mater. Today Energy* **9**, 1–10 (2018).
- ¹³ F. Biccari *et al.*, "Graphene-based electron transport layers in perovskite solar cells: A step-up for an efficient carrier collection," *Adv. Energy Mater.* **7**(22), 17013–17017 (2017).
- ¹⁴ P. Schulz, "Interface design for metal halide perovskite solar cells," *ACS Energy Lett.* **3**, 1287–1293 (2018).
- ¹⁵ A. Vassilakopoulou, D. Papadatos, and I. Katselas, "Flexible, cathodoluminescent and free standing mesoporous silica films with entrapped quasi-2D perovskites," *Appl. Surf. Sci.* **400**, 434–439 (2017).
- ¹⁶ C. Petridis, G. Kakavelakis, and E. Kyriakidis, "Renaissance of graphene-related materials in photovoltaics due to the emergence of metal halide perovskite solar cells," *Energy Environ. Sci.* **11**(5), 1030–1061 (2018).
- ¹⁷ E. Shi *et al.*, "Two-dimensional halide perovskite nanomaterials and nanostructures," *Chem. Soc. Rev.* **47**(16), 6046–6072 (2018).
- ¹⁸ F. Brivio, A. B. Walker, and A. Walsh, "Structural and electronic properties of hybrid perovskites for high-efficiency thin-film photovoltaics from first-principles," *APL Mater.* **1**(4), 042111 (2013).
- ¹⁹ Y. Wang *et al.*, "Density functional studies of stoichiometric surfaces of orthorhombic hybrid perovskite CH₃NH₃PbI₃," *J. Phys. Chem. C* **119**(2), 1136–1145 (2015).
- ²⁰ J. Haruyama *et al.*, "Termination dependence of stoichiometric CH₃NH₃PbI₃ surfaces for perovskite solar cells," *J. Phys. Chem. Lett.* **5**(16), 2903–2909 (2014).
- ²¹ I. E. Castelli *et al.*, "Bandgap calculation trends of organometal halide perovskites," *APL Mater.* **2**(8), 081514 (2014).
- ²² G. Volonakis and F. Giustino, "Fermi level of graphene-perovskite interfaces," *J. Phys. Chem. Lett.* **6**(13), 2496–2502 (2015).
- ²³ J. Haruyama *et al.*, "Surface properties of CH₃NH₃PbI₃ for perovskite solar cells," *Acc. Chem. Res.* **49**(3), 554–561 (2016).
- ²⁴ J. Haruyama *et al.*, "First-principles study of electron injection and defects at the TiO₂/CH₃NH₃PbI₃ interface of perovskite solar cells," *J. Phys. Chem. Lett.* **8**(23), 5840–5847 (2017).
- ²⁵ C. Quarti, F. De Angelis, and D. Beljonne, "Influence of surface termination on the energy level alignment at the CH₃NH₃PbI₃ perovskite/C₆₀ interface," *Chem. Mater.* **29**(3), 958–968 (2017).
- ²⁶ H. Uratani and K. Yamashita, "Charge carrier trapping at surface defects of perovskite solar cell absorbers: A first-principles study," *J. Phys. Chem. Lett.* **8**(4), 742–746 (2017).
- ²⁷ J.-C. Li *et al.*, "Interfacial interactions in monolayer and few-layer SnS/CH₃NH₃PbI₃ perovskite van der Waals heterostructure and their effects on electronic and optical properties," *ChemPhysChem* **19**(3), 291–299 (2017).
- ²⁸ W.-W. Yan *et al.*, "A first-principles prediction on the 'healing effect' of graphene preventing carrier trapping near the surface of metal halide perovskites," *Chem. Sci.* **9**, 3341–3353 (2018).
- ²⁹ I. Zhang *et al.*, "Interactions between molecules and perovskites in halide perovskite solar cells," *Sol. Energy Mater. Sol. Technol.* **175**, 1–19 (2018).
- ³⁰ J. Liu *et al.*, "Probing interfacial electronic properties of graphene/CH₃NH₃PbI₃ heterojunctions: A theoretical study," *Appl. Surf. Sci.* **440**, 35–41 (2018).
- ³¹ J. Zhao *et al.*, "Growth control, interface behavior, band alignment, and potential device applications of 2D lateral heterostructures," *Wiley Interdiscip. Rev.: Comput. Mol. Sci.* **8**, e1353 (2018).
- ³² L. Wang *et al.*, "Pb-activated amine-assisted photocatalytic hydrogen evolution reaction on organic-inorganic perovskites," *J. Am. Chem. Soc.* **140**, 1994–1997 (2018).

- ³³ Y. Li and Z. Chen, "XH/ π (X = C, Si) interactions in graphene and silicene: Weak in strength, strong in tuning band structures," *J. Phys. Chem. Lett.* **4**, 269–275 (2013).
- ³⁴ G. Kresse and J. Furthmüller, "Efficient iterative schemes for *ab initio* total-energy calculations using a plane-wave basis set," *Phys. Rev. B* **54**, 11169–11186 (1996).
- ³⁵ J. Klimeš, D. R. Bowler, and A. Michaelides, "Chemical accuracy for the van der Waals density functional," *J. Phys.: Condens. Matter* **22**, 022201–022205 (2010); "Van der Waals density functionals applied to solids," *Phys. Rev. B* **83**, 195131 (2011).
- ³⁶ T. Baikie, Y. Fang, J. M. Kadro, M. Schreyer, F. Wei, S. G. Mhaisalkar, M. Grätzel, and T. J. White, "Synthesis and crystal chemistry of the hybrid perovskite (CH₃NH₃PbI₃) for solid-state sensitized solar applications," *J. Mater. Chem. A* **1**, 5628–5641 (2013).
- ³⁷ P. Schulz, E. Edri, S. Kirmayer, G. Hodes, D. Cahen, and A. Kahn, "Interface energetics in organo-metal halide perovskite-based photovoltaic cells," *Energy Environ. Sci.* **7**, 1377–1381 (2014).
- ³⁸ P. Umari, E. Mosconi, and F. De Angelis, "Relativistic GW calculations on CH₃NH₃PbI₃ and CH₃NH₃SnI₃ perovskites for solar cell applications," *Sci. Rep.* **4**, 4467 (2014).
- ³⁹ F. Brivio, K. T. Butler, A. Walsh, and M. van Schilfgaarde, "Relativistic quasiparticle self-consistent electronic structure of hybrid halide perovskite photovoltaic absorbers," *Phys. Rev. B* **89**, 155204 (2014).
- ⁴⁰ M. L. Agiorgousis, Y.-Y. Sun, H. Zeng, and S. Zhang, "Strong covalency-induced recombination centers in perovskite solar cell material CH₃NH₃PbI₃," *J. Am. Chem. Soc.* **136**, 14570–14575 (2014).
- ⁴¹ H. J. Monkhorst and J. D. Pack, "Special points for Brillouin-zone integrations," *Phys. Rev. B* **13**, 5188–5192 (1976).
- ⁴² A. Poglitsch and D. Weber, "Dynamic disorder in methylammonium trihaloplumbates(II) observed by millimeter-wave spectroscopy," *J. Chem. Phys.* **87**, 6373–6378 (1987); C. C. Stoumpos, C. D. Malliakas, and M. G. Kanatzidis, "Semiconducting tin and lead iodide perovskites with organic cations: Phase transitions, high mobilities, and near-infrared photoluminescent properties," *Inorg. Chem.* **52**(15), 9019–9038 (2013).
- ⁴³ L. E. Orgel and J. D. Dunitz, "Stereochemistry of cupric compounds," *Nature* **177**, 462–465 (1957).
- ⁴⁴ Y. Lin, L. Shen, J. Dai, Y. Deng, Y. Wu, Y. Bai, X. Zheng, J. Wang, Y. Fang, H. Wei, W. Ma, X. C. Zeng, X. Zhan, and J. Huang, " π -conjugated Lewis base: Efficient trap-passivation and charge-extraction for hybrid perovskite solar cells," *Adv. Mater.* **29**(7), 1604545 (2016).
- ⁴⁵ B. Silvi and A. Savin, "Classification of chemical bonds based on topological analysis of electron localization functions," *Nature* **371**, 683–686 (1994); A. Savin, R. Nesper, S. Wengert, and T. F. Fässler, "ELF: The electron localization function," *Angew. Chem., Int. Ed. Engl.* **36**(17), 1808–1832 (1997).